Observation of thermospheric gravity waves in the Southern Hemisphere with GOLD

Scott L. England[1], Katelynn R. Greer[2], Stanley C. Solomon[3], Richard W. Eastes[2], William E. McClintock[2], Alan G. Burns[3]

[1] Aerospace and Ocean Engineering, Virginia Polytechnic Institute and State University, Blacksburg, Virginia, USA

[2] Laboratory for Atmospheric and Space Physics, University of Colorado Boulder, Boulder, Colorado, USA

[3] High Altitude Observatory, National Center for Atmospheric Research, Boulder, Colorado, USA

Corresponding author: Scott L. England (englands@vt.edu), Orcid: 0000-0001-5336-0040

Key Points

i. First observations of thermospheric gravity waves from a GOLD special operational mode campaign are presented

ii. Signatures of perturbations are seen to propagate northwards and appear to be atmospheric gravity waves

iii. Wave properties estimated from observations and GLOW model are consistent with a large-scale gravity wave

Abstract

The middle thermosphere from ~150 to 250 km is characterized by rapid increase in temperature with altitude and rapid ionization. The entire thermosphere is believed to be home to atmospheric waves that propagate through it, originating both in the atmospheric layers below and in the thermosphere itself. Within the middle thermosphere, direct observations of such waves are extremely sparse. The GOLD far-UV imaging spectrometer is able to observe the middle thermosphere from geostationary orbit. During October 2018 a special observational campaign was performed, designed to identify atmospheric waves. Signatures in the 135.6 nm O airglow were seen that move northwards with time, away from the Southern polar region. These are consistent with a large-scale atmospheric gravity wave. These results are the first time 135.6 nm airglow has been used to track such a wave and highlight the ability of GOLD to observe such waves, even when at a modest amplitude, and track their motion.

Plain Language Summary

The upper region of the Earth's atmosphere, stretching from around 90 – 500 km above the surface, is known as the thermosphere. In this region, the temperature generally increases with altitude, but the strongest increase is in a region known as the middle thermosphere. The main source of heating in this region is absorption of ultraviolet light from the sun, which also produces charged particles in this region, known as the ionosphere. Oscillations are observed in almost all the properties of the atmosphere at these altitudes, which are believed to result from waves within the atmosphere. In the middle thermosphere, there are very few direct observations of such waves. GOLD is a new instrument that can observe the middle thermosphere by measuring emissions from the atmosphere call airglow. During a day in October 2018, GOLD

observed what appear to be fluctuations in this airglow associated with such waves. The properties are determined, both from the GOLD observations, and a theoretical model.

1) Introduction

The middle thermosphere, from around 150 to 250 km altitude, is characterized by a rapid increase in temperature and changing atmospheric composition with altitude, high rates of photoionization and associated generation of photoelectrons. As in much of Earth's atmosphere, atmospheric waves are believed to play a key role in the dynamics of this region (e.g. Forbes, 2007). The spectrum of waves is observed to change at middle thermosphere altitudes, from the relatively small vertical wavelengths (10s km) seen in the mesosphere and lower thermosphere (MLT) to the relatively long vertical wavelengths (>100 km) seen in the upper thermosphere (e.g. Oliver *et al*, 1997; Djuth *et al*., 2010). Atmospheric gravity waves (GWs) are believed to be a key component of the wave spectrum in the middle thermosphere, and significantly impact this region, both in creating transient variations and in producing net acceleration, mixing, heating and heat flux as they dissipate (e.g. Yiğit and Medvedev, 2015). The GWs in the middle thermosphere are believed to be a mixture of waves originating in the lower regions of the atmosphere (both primary and secondary waves; e.g. Vadas and Fritts, 2006; Vadas and Liu, 2009; Yiğit *et al*., 2014) as well as waves generated in the thermosphere, primarily via Joule heating in the auroral regions (e.g. Richmond, 1978).

GWs in the MLT region have been observed frequently via a variety of methods, including images of airglow (e.g. Swenson and Mende, 1994), lidar (e.g. Wilson *et al*., 1991), radar (e.g.

Vincent and Fritts, 1987), observations of noctilucent clouds (e.g. Thurairajah *et al.,* 2017), and limb profiles from low-earth orbit spacecraft (e.g. Preusse *et al*., 2009). GWs have also been detected frequently with *in situ* observations in the upper thermosphere (e.g. Bruinsma and Forbes, 2008; Park *et al*. 2014; Garcia *et al*, 2016). Despite the strong impacts GWs are believed to have in the middle thermosphere (e.g. Vadas and Fritts, 2006; Vadas and Liu, 2009; Yiğit *et al*., 2014), very few direct observations of GWs in this region have been made. The vast majority of observations of GW at middle thermosphere altitudes come from radar observations of electron density or motion, which identify travelling ionospheric disturbances (TIDs) that are the ionospheric counterpart to the GW in the neutral atmosphere (e.g. Djuth *et al*., 2010; Negrea *et al*., 2016). Where observations of both the GW and TID have been made in the same location in the thermosphere, it has been shown that the TID may be a very good proxy for the underlying neutral GW (e.g. Earle *et al*., 2008), and thus observations of TIDs may provide a great deal of insight into the spectrum of GWs at this altitude, even if they don't reveal all the changes in the neutral atmosphere associated with the GW. Using a combination of ionospheric (airglow brightness) and thermospheric wind observations, Paulino *et al*., 2018 were able to deduce the intrinsic parameters of gravity waves in the middle thermosphere / bottom-side F-region and confirm that the waves seen in the ionospheric response were consistent with upward propagating gravity waves that are filtered by the background winds, both at these altitudes and below.

Determining the characteristics of GWs in the thermosphere is important for understanding the energy and momentum balance of this region. As just one example, it is believed that gravity waves propagated upwards from below can either heat or cool the thermosphere (e.g. Yiğit and Medvedev, 2009; Vadas *et al*., 2014), but their impact on the thermosphere depends on their properties, as well as the mean state. The characteristics of TIDs observed are typically grouped into two categories according to their horizontal spatial scales. Medium scale TIDs (MSTIDs), with horizontal wavelengths around 100 – 500 km, and horizontal phase speeds of around 100 – 200 m/s are believed to be associated with primary or secondary GWs from the lower levels of the atmosphere (e.g. Azeem *et al*, 2017), whereas large scale TIDs (LSTIDs), with horizontal wavelengths over 1000 km, and horizontal phase speeds of around 500 m/s are believed to be associated with aurorally-generated GWs (e.g. Bruinsma *et al*., 2006). Given the importance of GWs in the middle thermosphere, and the comparative lack of direct observations of these waves in this region, further examination of observations of GWs in the neutral atmosphere at these altitudes is warranted.

Global-scale Observations of the Limb and Disk (GOLD) is a NASA Mission of Opportunity, primarily focused on observing the far-ultraviolet airglow emissions from the Earth's middle thermosphere and F-region ionosphere. Here we present the results from a special campaign of observations from GOLD, designed to reveal the impacts of GWs on the airglow originating from the middle thermosphere. While this dataset is unique in that it represents a special campaign that has yet to be repeated, these results will highlight the capabilities of the GOLD instrument to observe such waves. We identify the impact GWs on the FUV airglow during a geomagnetically quiet to moderate day, analyze the GOLD observations and make use of an airglow model to estimate the intrinsic wave parameters in the neutral atmosphere. These results can also be used to help define future campaigns with the GOLD instrument.

2) Experimental Setup and Data

GOLD is a 2-channel far-ultraviolet imaging spectrometer that observes the Earth from onboard the SES-14 geostationary communications satellite, which is located at 312.5° longitude (Eastes *et al*., 2017; McClintock *et al*., 2017; Eastes *et al*., 2019). During regular operations, when the disk of the Earth is illuminated by the sun, the instrument scans the disk of the Earth, building up an image of the Earth's disk with a 30-minute cadence. GOLD makes observations between ~134 and 167 nm, which allows identification of the prominent dayglow features of O at 135.6 nm and LBH band of N_2. During early operations on October 13, 2018, both channels of the instrument performed a special mode campaign, designed to identify the impacts of atmospheric waves on the middle thermosphere. Based on modeling by Greer *et al*., [2018], the anticipated changes in O dayglow at 135.6 nm were of order ±2 Rayleighs, requiring an integration time of ~400 s to clearly identify such perturbations, which is much longer than the typical dwell time when scanning the disk. To maximize the chance of seeing such a perturbation in the airglow, the special mode campaign involved pointing both channels close to nadir, with the mirror position set to view the southern hemisphere and stare continuously from ~12 – 18 hours UTC (see Figure 1a). As the two channels are mounted in opposite directions on the spacecraft, the tilt of the slit with latitude is in the opposite direction for each channel such that the longitudinal separation of the fields of view is ~1° at the equator, increasing to ~9.9° towards the edge of the disk at -61° latitude. It is this, currently unique ~6-hour long dataset that will be considered here.

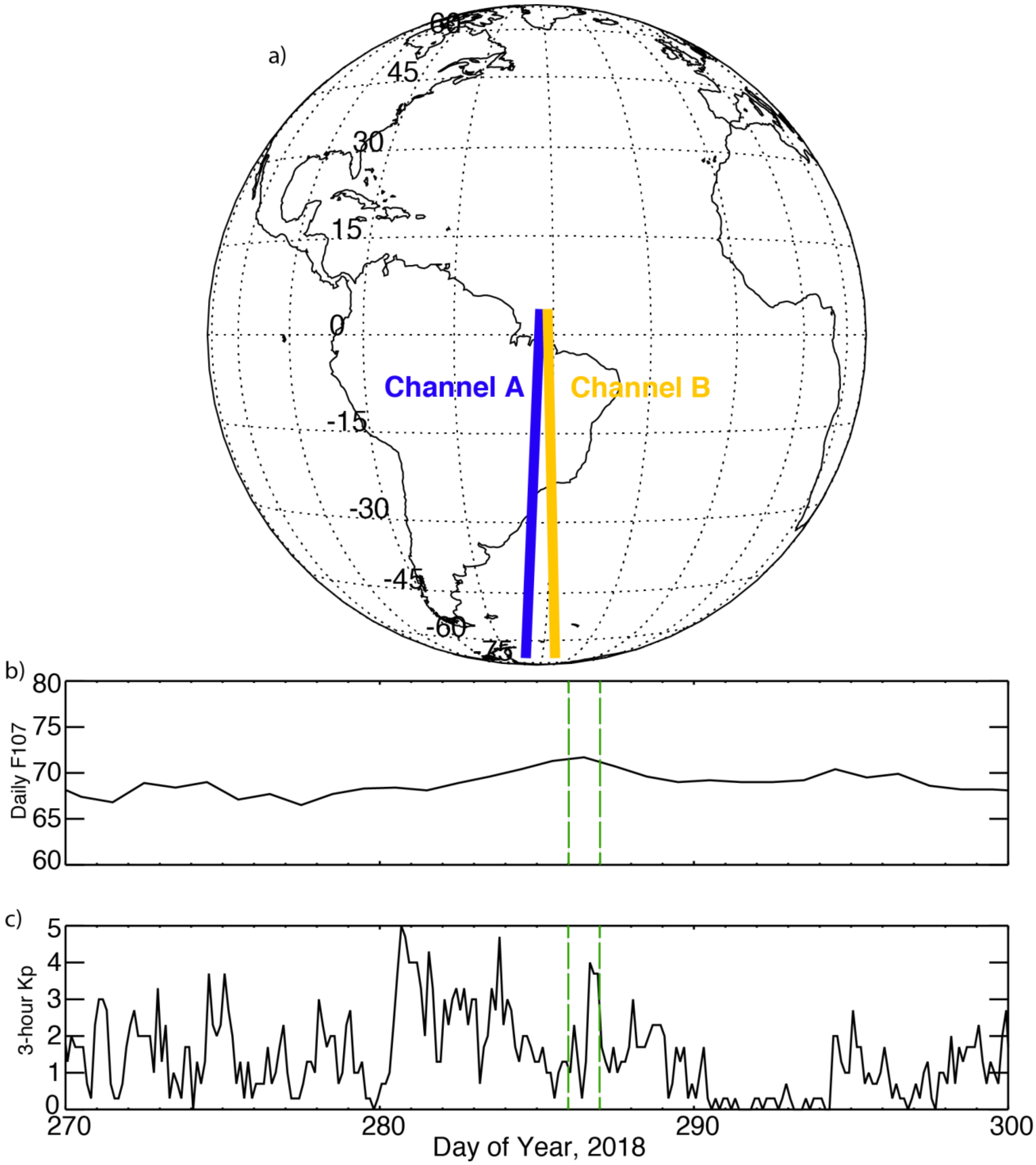

Figure 1: Panel a shows the fields of view of Channel A and B of GOLD during the special mode campaign on October 13, 2018. Panel b shows daily F10.7 index and panel c shows the 3-hourly

K_p index around the time of this campaign, with October 13, 2018 highlighted by the vertical dashed lines.

While the special mode campaign was pre-planned and not intended to align with any specific geophysical conditions, the conditions present on October 13, 2018 were geomagnetically quiet to moderate. Figure 1b and 1c show the F10.7 and Kp indices during this period of 2018. F10.7 values on the day was low at 71.7 10^{-22} W m^{-2} Hz^{-1}, while the Kp values show moderate activity, reaching 4+ by later in the day. Examining the real-time auroral AE index shows activity below 100 nT from 12 – 15 UT, with a pickup between 15 – 18 UT up to over 1200 nT by the end of the period. It is worth noting that this heightened activity occurred several hours into the campaign.

This study focuses on Level 1b and 1c (L1b & L1c) data from the GOLD instrument, which are described in the Data Products Users Guide (see https://gold.cs.ucf.edu). The L1b files are available for this campaign at 2-minute cadence and provide the spectrum in instrument counts vs wavelength and latitude. The L1b processing includes geometric corrections for the detector and optics, filtering of the counts based on the detector pulse heights, a correction based on the detector deadtime (maximum count rate) and data are binned on a regular wavelength scale. The L1c files are available at a 10-minute cadence and provide the spectrum in radiance vs wavelength and latitude. The L1c processing additionally includes the radiometric conversion based on knowledge of the instrument flatfield response, scattered light and dark current noise sources, and sensitivity vs wavelength.

3) Data Analysis

Given the low amplitude of the signal expected from an atmospheric gravity wave described above, our analysis focuses on the bright O doublet feature near 135.6 nm, although it is worth noting that this overlaps the (3,0) emission from N_2 at 135.4 nm. Some of this can be excluded by not including the shortest wavelength bins in our computation of the 135.6 nm feature, as has been done here. To identify the perturbations associated with any atmospheric fluctuations such as gravity waves, we first isolate the 135.6 nm airglow from the background, then detrend the variations associated with changes in local time and any that may be associated with changes in solar EUV brightness. This is done in three steps. To isolate the 135.6 nm airglow, we add up the signal at each pixel at each point in time in the range from 135.2 – 136.0 nm, and perform a background subtraction using two out of band regions either side of this, at 134.4 – 134.8 and 136.4 – 136.8 nm (see Figure 2a). To remove the local time variations, a third-order polynomial fit is made to the signal at each pixel in each channel, and this smoothly varying signature is removed (see Figure 2b). Finally, changes associated with varying solar EUV brightness affect the signal at all latitudes on the disk simultaneously. As such, these are easily identified and removed by finding and removing the mean value of brightness across the image, after the local time variation is removed. This leaves a residual signal whose mean value is zero.

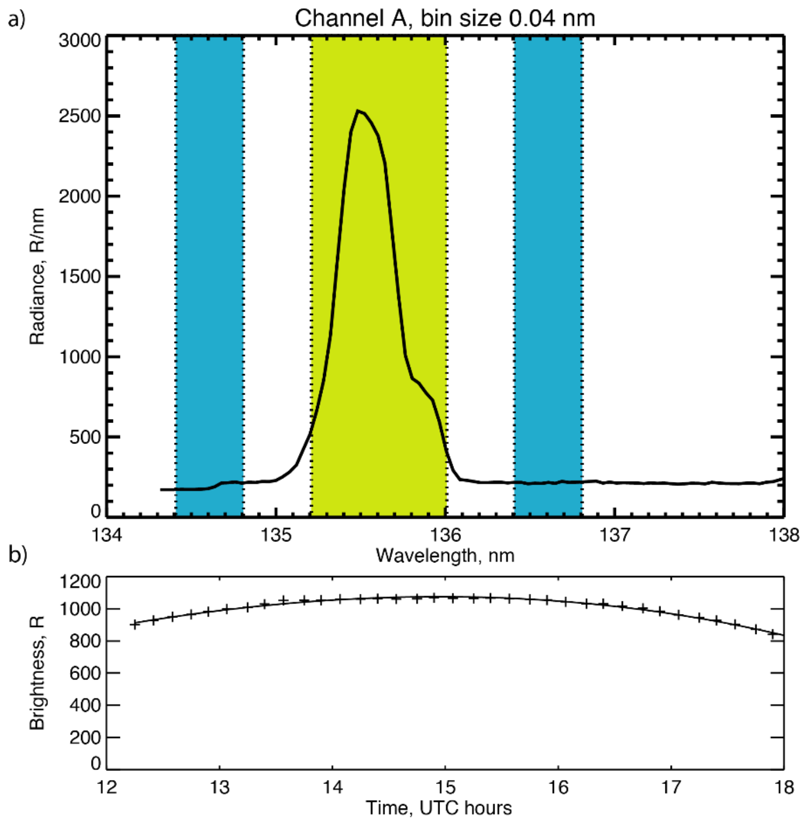

Figure 2: Panel a shows an example spectrum from the L1c data from Channel A at -39° latitude, 12:49 – 12:58 UTC. The area highlighted in green represents the in-band and those in blue represent the out-of-band signals used in the analysis. Panel b shows the variation in the 135.6 nm signal as a function of time for the same pixel shown in panel a. The plus symbols represent the L1c values at 10-minute cadence, and the solid line shows the 3rd order polynomial least-squares fit to these data.

The atmospheric wave perturbations that may be expected in the middle thermosphere have periods of 10s of minutes to several hours, so both the 2-minute cadence L1b and 10-minute cadence L1c data should have sufficient temporal resolution to capture these. At this 2-minute cadence, the L1b residuals are extremely noisy. To allow any longer-period signatures to be seen, we perform a 10-minute rolling median filter on these residuals at each latitude. This removes outlying high and low data points, and puts these data on approximately the same temporal resolution as the L1c file. Figure 3 shows residuals for L1b and L1c for 2 channels, after this median filter applied to L1b. In the residuals from both channels and both the L1b and L1c data, perturbations that appear to move northwards with time are seen. Perhaps most clearly visible are a pair of higher count rates / brightnesses features between 12 – 14 hours UTC near -50 – -65° latitude. The locations of these were determined by eye and their locations are given in Table 1.

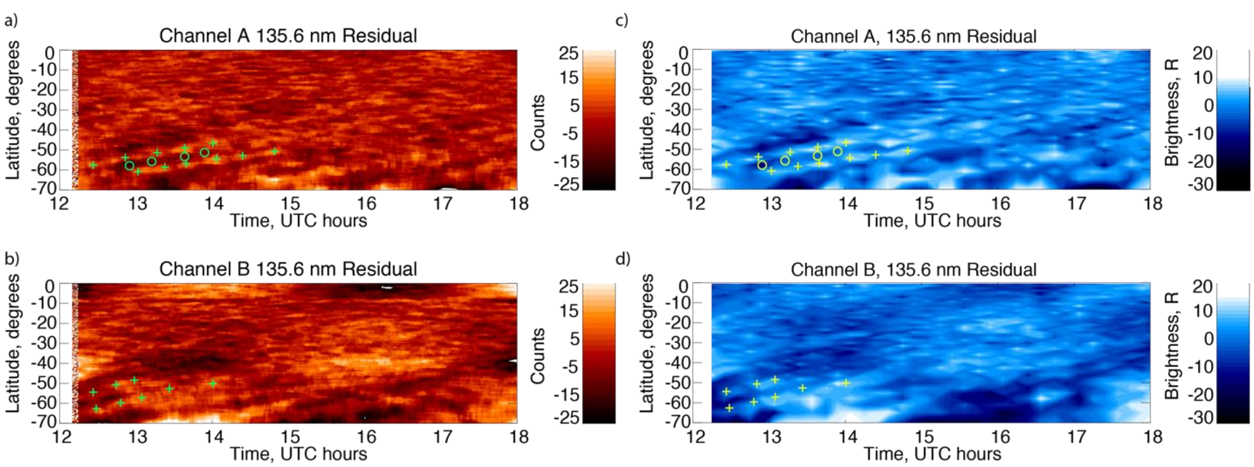

Figure 3: Panels a and b show the residual counts as defined in the text in the L1b data for Channels A and B respectively as functions of time and latitude. A 10-minute rolling median filter has been applied at each latitude for the L1b data. Panels c and d are as a and b, but for the brightness in Rayleighs from the L1c data. The locations of the apparent wave features, marked by the plus and circle symbols, are given in the Supplementary Data.

Channel	Feature	Time, UTC hours	Latitudes, degrees
A	First	12.44	-57.52

	wave peak	12.86	-53.78
		13.28	-51.34
		13.64	-48.9
		14.01	-46.63
A	Second wave peak	13.03	-60.77
		13.38	-58.49
		13.66	-56.87
		14.06	-54.27
		14.4	-52.81
		14.82	-50.69
A	Trough	12.91	-57.71
		13.21	-55.57
		13.64	-53.13
		13.9	-51.1
B	First wave peak	12.48	-62.63
		12.8	-59.63
		13.08	-57.14
		13.44	-52.64
		14.01	-50.05
B	Second wave peak	12.44	-54.39
		12.84	-50.64
		13.08	-48.4

Table 1: The locations of the wave peak and trough feature highlighted in Figure 3.

Assuming that the two channels are seeing the same feature in the atmosphere, which seems reasonable given the apparent similarity for the pair of features described above, and furthermore assuming this to be an atmospheric wave with plane wave fronts, it is possible to estimate a number of wave parameters. The mean residual brightness at the peak locations in Channel A for the first wave is 3.4 R and for the second wave is 6.0 R. The mean residual brightness for the trough between these waves is – 5.9 R. The mean observed brightness in this region is 1180 R, so using the average of the two peaks and the trough values listed above, the wave amplitude is around 0.45 % , or 10.6 R. Performing a linear least-squares fit to the locations of the peaks of these two waves in both channels, we can determine the wave period by the time between the two peaks arriving at -52° latitude (chosen as both channels see both waves in this region). The estimated wave period from Channel A is 1.3 hours and from Channel B is 1.0 hours, with a mean of 1.2 hours. From the same linear fits, the meridional phase speed is estimated to be 7.6° / hour northwards or ~230 m/s. The peaks of the waves appear to reach -52° latitude 0.7 hours earlier in Channel B than Channel A. Combining this with the longitudinal separation of Channels A and B at this latitude being 7.7° leads to an estimate of the zonal phase speed as 11° / hour westwards or ~270 m/s. Using the meridional and zonal phase speeds, the total horizontal phase speed is estimated to be 360 m/s, with an azimuth of wave propagation of 300°. From the phase speeds and period, the horizontal wavelength is estimated to be ~1500 km. These wave properties will be discussed further in Sections 4 and 5.

4) Airglow simulations

From the measured amplitude of the brightness perturbation, it is possible to estimate the amplitude of a gravity wave that would be required to produce such a signature. Following the methodology of Greer *et al.*, [2018], we use a background atmosphere from the thermosphere-ionosphere-electrodynamics GCM (TIEGCM v2.0; Maute, 2017) and the Global Airglow model (GLOW; Solomon, 2017) to simulate the 135.6 nm O and (3,0) N_2 airglow GOLD would observe at -50° latitude for the conditions present on October 13, 2018. This is then perturbed with a sinusoidal function that modifies the atmospheric density and temperature, as described in Section 2 of Greer *et al.*, [2018]. By varying the amplitude of this perturbation, we can find the amplitude of a wave in the middle thermosphere that would produce a perturbation in the airglow of the same amplitude as observed by GOLD. Figure 4 shows the results of seven simulations at varying wave amplitude, at both 9 am and 12 pm local time (corresponding approximately to 12 and 15 UT in the GOLD observations). At these relatively small-amplitude perturbations in the atmosphere, the response in the airglow is very close to linear, and a linear least-squares fit is used to identify the best-fit wave amplitude that corresponds to the observed airglow signature. The 10.6 R or 0.9 % peak-to-trough variation seen by GOLD near these local times could be explained by a wave with an amplitude of 34 K, corresponding to 8.5 % density fluctuation.

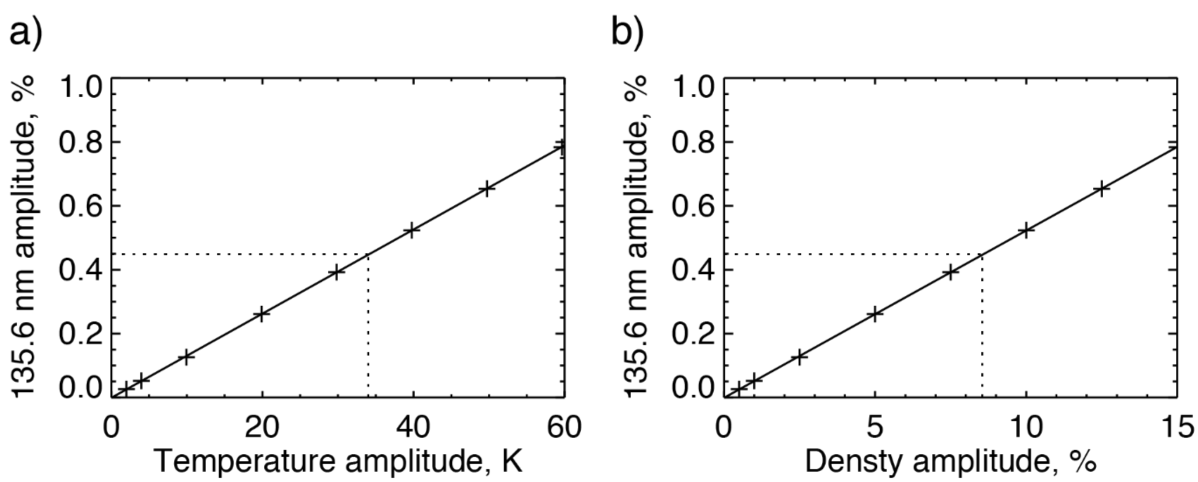

Figure 4: Results of the GLOW airglow simulations of the O 135.6 nm double and N_2 (3,0) at -50° latitude for the conditions present on October 13, 2018. The amplitude of the simulated airglow perturbation is shown as a function of the change in the neutral atmosphere, expressed in terms of (panel a) the temperature and (panel b) the density perturbations. Simulations correspond to an average of 12:00 and 15:00 UT. The solid lines show the linear least-squares fit to these data. The dotted line shows the amplitude of the airglow perturbation observed by GOLD.

It is worth noting that the 135.6 nm O dayglow also includes a minor contribution from O^+ radiative recombination. This is expected to be small at -50° latitude, but nonetheless it is worth determining if an ionospheric perturbation, either instead of in addition to an atmospheric perturbation could explain the GOLD observations. Using an estimate of the ionospheric O^+ density in the region of the observed wave from IRI-2016 (Bilitza, 2018), and the radiative recombination airglow coefficients from Melèndez-Alvira *et al*., (1999), the total brightness of O^+ radiative recombination near 12 UT is estimated to be 20 R. Thus, only an extremely large amplitude variation in O^+ in the ionosphere could produce the 10.6 R variation seen by GOLD. While it is likely that some portion of the observed signature is associated with ionospheric O^+ perturbations, it seems likely that the majority of the observed signal is associated with variations in the neutral middle thermosphere.

5) Discussion and Conclusions

During the observing campaign on October 13th, 2018, GOLD observed perturbations in the 135.6 nm dayglow in the Southern hemisphere. These perturbations in the brightness of the airglow were seen to move northwards with time and were seen with both channels of the instrument, providing confidence that they represent the response to structures in the thermosphere. The structures appear to be atmospheric gravity waves, or TAD, and if so this would be the first time that the properties of such waves, including their propagation, have been identified in 135.6 nm airglow. Using data from both channels, and approximating the wave as plane wave it is possible to identify the best-fit horizontal wavelength of 1500 km, period of 1.2 hours, phase speed of 360 m/s and azimuth of propagation of 300°. These characteristics are broadly consistent with those reported for large-scale TADs seen in the upper thermosphere (e.g. Bruinsma *et al*., 2006), and the larger scale TIDs seen in the ionosphere at middle-thermosphere altitudes (e.g. Negrea *et al.*, 2016). Utilizing a model of the airglow, it is possible to estimate the approximate amplitude of the atmospheric perturbation associated with this wave. The best fit to the observed airglow perturbation was found from a wave in the neutral atmosphere with a temperature amplitude of 33 K and a density amplitude of 8.5 %, which is consistent with *in situ* observations of TADs in the middle – upper thermosphere (e.g. Earle *et al*., 2008).

The direction of propagation suggests a wave source that is south and east of the observed region, i.e. to the east of the Antarctic Peninsula. The GOLD data does not uniquely identify the wave source, but there are perhaps three types broad source locations one could consider – gravity waves of tropospheric origin (primary gravity waves), secondary gravity waves produced at some higher altitude where a primary wave dissipates, or waves of thermospheric origin. As described in Azeem *et al*., [2017] (following Vadas, 2013), the maximum phase speed for a wave of tropospheric origin is around 255 m/s, which appears to exclude this as the direct origin of the wave observed by GOLD, leaving the other two as possibilities in this case. Comparison to other observations, such as from ground-based instrumentation would be one possible way to determine the wave source, but is beyond the scope of this study.

The results highlight the ability of GOLD to observe atmospheric waves. From its geostationary vantage point, GOLD is perhaps ideally suited to tracking such waves over large horizontal distances. The ability to detect a wave of relatively modest amplitude, not in response to a geomagnetic storm, suggests opportunities for similar observing campaigns to be planned in the future. GOLD’s field of regard includes several regions believed to be important sources of atmospheric gravity waves, including the Andes mountain range, the Antarctic Peninsula and strong convective sources over the Amazon rainforest.

Acknowledgements, Samples and Data

The GOLD data are available from the GOLD Science Data Center (http://gold.cs.ucf.edu/search/) and NASA's Space Physics Data Facility (https://spdf.gsfc.nasa.gov). The Kp and F10.7 data are available from NASA's OMNIWeb (https://omniweb.gsfc.nasa.gov). The IRI-2016 calculations were performed using NASA's CCMC (https://ccmc.gsfc.nasa.gov). the AE real-time data are available from http://wdc.kugi.kyoto-u.ac.jp/ae_realtime/201810/index_20181013.html. This research was supported by NASA contract 80GSFC18C0061.

6) References

- Azeem, I., S. L. Vadas, G. Crowley, and J. J. Makela (2017), Traveling ionospheric disturbances over the United States induced by gravity waves from the 2011 Tohoku tsunami and comparison with gravity wave dissipative theory, J. Geophys. Res. Space Physics, 122, 3430–3447, doi:10.1002/2016JA023659.
- Bilitza, D. (2018), IRI the International Standard for the Ionosphere, Adv. Radio Sci., 16, 1-11, https://doi.org/10.5194/ars-16-1-2018.
- Bruinsma, S., J. M. Forbes, R. S. Nerem, and X. Zhang (2006), Thermosphere density response to the 20–21 November 2003 solar and geomagnetic storm from CHAMP and GRACE accelerometer data, J. Geophys. Res., 111, A06303, doi:10.1029/2005JA011284.
- Bruinsma, S. L., & Forbes, J. M. (2008). Medium- to large-scale density variability as observed by CHAMP. Space Weather, 6, S08002. https://doi. org/10.1029/2008SW000411

- Djuth, F. T., L. D. Zhang, D. J. Livneh, I. Seker, S. M. Smith, M. P. Sulzer, J. D. Mathews, and R. L. Walterscheid (2010), Arecibo's thermospheric gravity waves and the case for an ocean source, J. Geophys. Res., 115, A08305, doi:10.1029/2009JA014799.
- Earle, G. D., A. M. Musumba, and S. L. Vadas (2008), Satellite-based measurements of gravity wave-induced midlatitude plasma density perturbations, J. Geophys. Res., 113, A03303, doi:10.1029/2007JA012766.
- Eastes, R. W., McClintock, W. E., Burns, A. G., Anderson, D. N., Andersson, L., Codrescu, M., et al. (2017). The Global-Scale Observations of the Limb and Disk (GOLD) mission. Space Science Reviews, 212(1-2), 383–408. https://doi.org/10.1007/s11214-017-0392-2
- Eastes, R. W., Solomon, S. C., Daniell, R. E., Anderson, D. N., Burns, A. G., England, S. L., et al. (2019). Global-scale observations of the equatorial ionization anomaly. *Geophysical Research Letters*, *46*. https://doi.org/ 10.1029/2019GL084199
- Forbes, J.M. (2007). Dynamics of the Thermosphere, Journal of the Meteorological Society of Japan, Vol. 85B, pp. 193—213.
- Garcia, R. F., Bruinsma, S., Massarweh, L., & Doornbos, E. (2016). Medium-scale gravity wave activity in the thermosphere inferred from GOCE data. Journal of Geophysical Research: Space Physics, 121, 8089–8102. https://doi.org/10.1002/2016JA022797
- Greer, K. R., England, S. L., Becker, E., Rusch, D., & Eastes, R. (2018). Modeled gravity wave-like perturbations in the brightness of far ultraviolet emissions for the GOLD mission. Journal of Geophysical Research: Space Physics, 123, 5821–5830. https://doi.org/10.1029/2018JA025501

- Maute, A., Thermosphere–ionosphere-electrodynamics general circulation model for the Ionospheric Connection Explorer: TIEGCM-ICON. Space Sci. Rev. (2017), doi:10.1007/s11214-017-0330-3
- McClintock, W. E., et al. (2017), Global-scale Observations of the Limb and Disk (GOLD): science implementation. American Geophysical Uniton Fall Meeting, SA31A-2561.
- Melèndez-Alvira, D. J., R. R. Meier, J. M. Picone, P. D. Feldman, and B. M. McLaughlin (1999), Analysis of the oxygen nightglow measured by the Hopkins Ultraviolet Telescope: Implications for ionospheric partial radiative recombination rate coefficients, J. Geophys. Res., 104, 14,901–14,914.
- Negrea, C., N. Zabotin, T. Bullett, T. Fuller-Rowell, T.-W. Fang, and M. Codrescu (2016), Characteristics of acoustic gravity waves obtained from Dynasonde data, J. Geophys. Res. Space Physics, 121, 3665–3680, doi:10.1002/ 2016JA022495.
- Oliver, W. L., Y. Otsuka, M. Sato, T. Takami, and S. Fukao (1997), A climatology of F region gravity wave propagation over the middle and upper atmosphere radar, J. Geophys. Res., 102, 14,499.
- Park, J., Lühr, H., Lee, C., Kim, Y. H., Jee, G., & Kim, J.-H. (2014). A climatology of medium-scale gravity wave activity in the midlatitude/low- latitude daytime upper thermosphere as observed by CHAMP. Journal of Geophysical Research: Space Physics, 119, 2187–2196. https://doi. org/10.1002/2013JA019705
- Paulino, I., Moraes, J.F., Maranhão, G.K., Wrasse, C.M., Buriti, R.A., Medeiros, A.F., Paulino, A.R., Takahashi, H., Makela, J.J., Meriwether., J.W., and Compos, J.A.V. (2018), Intrinsic parameters of periodic waves observed in the OI6300 airglow layer over the

Brazilian equatorial region, Ann. Geophys., 36, 265-273m https://doi.org/10.5194/angeo-36-265-2018.

- Preusse, P., S. D. Eckermann, M. Ern, J. Oberheide, R. H. Picard, R. G. Roble, M. Riese, J. M. Russell, and M. G. Mlynczak (2009), Global ray tracing simulations of the SABER gravity wave climatology, *J. Geophys. Res.*, *114*, D08126, doi:10.1029/2008JD011214.
- Richmond, A. D. (1978). Gravity wave generation, propagation, and dissipation in the thermosphere. Journal of Geophysical Research, 83(A9), 4131–4145. https://doi.org/10.1029/JA083iA09p04131
- Solomon, S. C. (2017). Global modeling of thermospheric airglow in the far ultraviolet. Journal of Geophysical Research: Space Physics, 122, 7834–7848. https://doi.org/10.1002/2017JA024314
- Swenson, G. R., and S. B. Mende, OH emission and gravity waves (including a breaking wave) in all-sky imagery from Bear Lake, UT, *Geophys. Res. Lett.*, *21*, 2239–2242, 1994.
- Thurairajah, B., Sato, K., Yue, J., Nakamura, T., Kohma, M., Bailey, S.M., and Russell III, J.M. (2017). Simultaneous observation of gravity waves at PMC altitude from AIM/CIPS experiment and PANSY radar over Syowa (69°S, 39°E), J. Atmos. Sol. Terr. Phys., 164, 324-331, https://doi.org/10.1016/j.jastp.2017.10.006
- Vadas S.L., Fritts D.C. (2006) Influence of solar variability on gravity wave structure and dissipation in the thermosphere from tropospheric convection. J Geophys Res 111:A10S12. doi:10.1029/2005JA011510
- Vadas S.L., Liu H.-L. (2009) The generation of large-scale gravity waves and neutral winds in the thermosphere from the dissipation of convectively-generated gravity waves. J Geophys Res 114:A10310. doi:10.1029/2009JA014108

- Vadas, S. L. (2013), Compressible f-plane solutions to body forces, heatings, and coolings, and application to the primary and secondary gravity waves generated by a deep convective plume, J. Geophys. Res. Space Physics, 118, 2377–2397, doi:10.1002/jgra.50163.
- Vadas, S. L., Liu, H. L., & Lieberman, R. S. (2014). Numerical modeling of the global changes to the thermosphere and ionosphere from the dissipation of gravity waves from deep convection. *Journal of Geophysical Research: Space Physics*, *119*(9), 7762-7793.
- Vincent, R. A., and D. C. Fritts, A climatology of gravity waves in the mesosphere and lower thermosphere over Adelaide, Australia, *J. Atmos. Sci.*, *44*, 748–760, 1987.
- Wilson, R., M.-L. Chanin, and A. Hauchecorne, Gravity waves in the middle atmosphere observed by Rayleigh lidar, part 2, Climatology, *J. Geophys. Res.*, *96*, 5169–5183, 1991
- Yiğit, E., & Medvedev, A. S. (2009). Heating and cooling of the thermosphere by internal gravity waves. *Geophysical Research Letters*, *36*(14).
- Yiğit, E. and A.S. Medvedev (2015). Internal wave coupling processes in Earth's atmosphere, Adv. Space Res., 55 (4) 983-1003, 10.1016/j.asr.2014.11.020
- Yiğit, E., A. S. Medvedev, S. L. England, and T. J. Immel (2014), Simulated variability of the high-latitude thermosphere induced by small-scale gravity waves during a sudden stratospheric warming, *J. Geophys. Res. Space Physics*, *119*, 357–365, doi:10.1002/2013JA019283.